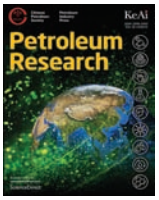
Petroleum Research 11 (2026) 799–814

Contents lists available at ScienceDirect

Petroleum Research

journal homepage: http://www.keaipublishing.com/en/journals/petroleum-research/



Full Length Article

The impact of grid refinement, foam model, and peaceman model on gas and liquid injectivities during SAG foam EOR: An FFT benchmarking study

Rodrigo O. Salazar Castillo [a,*], Lily Qian [b], Bibiana Téllez García [c], William R. Rossen [d]

[a] Instituto Mexicano del Petróleo, Gerencia de Investigación en Explotación, Eje Central Lázaro Cárdenas 152, San Bartolo Atepehuacan, Gustavo A. Madero, 07730, Mexico City, Mexico
[b] Harvard Business School, 02163 Soldiers Field Rd, Boston, MA, United States of America
[c] Instituto Nacional de Astrofísica, Óptica y Electrónica, Calle Luis Enrique Erro No. 1 Santa María Tonanzintla, 72840, Puebla, Mexico
[d] Department of Geoscience and Engineering, Delft University of Technology, Stevinweg 1, 2628 CN, Delft, the Netherlands

ARTICLE INFO

Article history:
Received 19 February 2025
Received in revised form
10 December 2025
Accepted 11 December 2025
Available online 18 December 2025

Keywords:
Foam injectivity
Reservoir simulation
Surfactant-alternating-gas process
Fractional-flow theory
Grid refinement
Enhanced oil recovery

ABSTRACT

Surfactant-Alternating-Gas (*SAG*) utilizes foam to reduce gas mobility and improve reservoir sweep efficiency in gas-injection enhanced oil recovery and carbon capture and storage. Although *SAG* is known to have many benefits that increase hydrocarbon recovery, liquid injectivity is typically very poor during a *SAG* process. Conventional foam simulators use the Peaceman model to estimate injection-well pressure. However, because they assume uniform saturation in the grid block, they do not account for near-wellbore saturation distribution that improves gas and liquid injectivities during a *SAG process*. We use a conventional foam simulator to test the impact of grid refinement on injectivity. We compare simulation results to those with fractional-flow theory (*FFT*) using the a model very widely used in simulations. In addition, we test the effect of complete foam collapse at irreducible water saturation (S_{wr}), of neglecting the Peaceman model, and of disallowing foam in the injector grid block. We compare the transient behaviors and the average injectivities, calculated during one pore volume of injected fluid. Our results show that in a conventional simulation (including the Peaceman model) grid refinement increases gas and liquid injectivities. However, the results do not match *FFT* predictions. The assumption of complete foam collapse at S_{wr} increases gas injectivity (still without matching *FFT* results); however, it has a smaller impact on liquid injectivity and grid refinement results in an increase in gas and liquid injectivities. Excluding the Peaceman model reduces the error in simulated injectivities at coarse grid refinements but still without matching the *FFT* prediction. Finally, the procedure of excluding foam in the injection-well grid block gives average injectivities like our *FFT* calculations without requiring extraordinary grid refinement.

© 2025 Chinese Petroleum Society. Publishing services by Elsevier B.V. on behalf of KeAi Communications Co. Ltd. This is an open access article under the CC BY-NC-ND license (http://creativecommons.org/licenses/by-nc-nd/4.0/).

1. Introduction

Foam reduces gas mobility in gas-injection enhanced oil recovery (*EOR*) (Kovscek et al., 1995; Lake et al., 2014; Rossen, 1996) and carbon capture and storage (Orujov et al., 2023; Rossen et al., 2022). It does so by trapping gas in place and greatly increasing resistance to the flow of flowing gas encased in bubbles. This increases the macroscopic sweep efficiency of gas by mitigating gravity segregation (Jamshidnezhad et al., 2010) and diverting flow from high-permeability to low-permeability layers (Al Ayesh et al., 2017). A standard method of foam injection is Surfactant-Alternating-Gas (*SAG*), also known as FAWAG, where foam is created in the reservoir by the alternating injection of slugs of liquid with dissolved surfactant and gas (Blaker et al. 2002). This method offers better injectivity than direct foam injection and avoids the safety and corrosion problems of handling simultaneous injection in the facilities (Heller, 1994; Shan and Rossen, 2004). Even though this injection method increases gas

* Corresponding author.
E-mail addresses: rosalazar@imp.mx, rodrigo.foton@gmail.com (R.O. Salazar Castillo).

Peer review under the responsibility of Editorial Office of Petroleum Research.

https://doi.org/10.1016/j.ptlrs.2025.12.001
2096-2495/© 2025 Chinese Petroleum Society. Publishing services by Elsevier B.V. on behalf of KeAi Communications Co. Ltd. This is an open access article under the CC BY-NC-ND license (http://creativecommons.org/licenses/by-nc-nd/4.0/).

injectivity, liquid injection remains poor (Kuehne et al., 1990; Martinsen and Vassenden, 1999). There is yet no complete model for liquid injectivity during SAG. Gong et al. (2020a) conducted core-flood experiments to reveal how near-wellbore conditions affect gas and liquid injectivity during SAG. They show that gas and liquid injectivity are the consequence of the propagation of multiple banks. During gas injection, there are two banks: a foam bank followed by a collapsed-foam bank. During liquid injection, there are three banks: the collapsed-foam bank, surrounded by a gas-dissolution bank and a liquid-fingering bank. No simulator yet incorporates these effects.

Conventional foam simulators use the Peaceman model to estimate the injection-well pressure during liquid and gas injection. Gong et al. (2019) conclude that conventional foam simulators do not account for the propagation of the collapsed-foam bank, liquid fingering or gas dissolution. Their results indicate that the Peaceman equation significantly underestimates gas and liquid injectivity during SAG in a 100 m $\times$ 100 m grid block. Several field-scale simulation studies (Agada et al., 2015; AlMaqbali et al., 2015; Masoudi et al., 2015) have used grid blocks roughly 15 m $\times$ 15 m in size without grid refinement around the injection well. Other studies (Mukherjee et al., 2015; Sharma et al., 2017) have incorporated grid refinement to better reproduce gas and liquid injectivity during SAG, where the dimensions of the grid block containing the injection well were reduced to as small as 0.61 m $\times$ 0.61 m, but the effect on injectivity was not further discussed. However, incorporating grid refinement has not solved the problem of reproducing injectivity accurately (Quinelato et al., 2022). The difficulty in modeling injectivity during gas injection is partly due to the dry-out effect, where foam mobility abruptly rises as it dries out (Leeftink et al., 2015). Sharma (2019) assigned a value of foam parameter *fmmob* of zero in the injection-well grid block to mimic this effect by disallowing foam within a radius of 5 ft ($\approx$1.5 m) around the injector. Doing so increases estimated injectivity, but the impact of this procedure has not yet been tested against analytical tools such as fractional-flow theory (*FFT*).

In this paper, we investigate the effect of refining the grid around the injection well on the accuracy of estimated injection pressure for gas and liquid injection in a *SAG* process for the first gas slug and second liquid slug. For the purposes of this comparison, we assume the STARS foam interpolation model adequately represents foam behaviour under the laboratory and idealised conditions considered; nevertheless, limitations of this assumption are discussed below. In addition, we do not incorporate the mechanisms observed experimentally by Gong et al. (2019, 2020b, 2024) that are not included in the simulator. The *STARS* model allows for limited effect of dry-out, but does not represent complete foam collapse at any water saturation. Foam collapse upon dry-out is a reflection of the limiting capillary pressure (Khatib et al., 1988). This effect is fundamental to current foam models (Boeije and Rossen, 2015a,b; Cheng et al., 2000; Kovscek et al., 1995; Zhou and Rossen, 1995). Foam must collapse completely if capillary pressure reaches extremely high values at irreducible water saturation S_{wr}. If not, foam may not collapse completely at S_{wr}. Namdar Zanganeh et al. (2014) proposed modifying the *STARS* model to keep behaviour unchanged over most foam qualities but give complete foam collapse at S_{wr}. We investigate the effect of the Namdar-Zanganeh (*NZ*) correction in refined-grid scenarios to evaluate its contribution to better reproducing injectivity. Finally, we consider the role of setting the parameter *fmmob* to zero in the grid block containing the injection well to study its contribution to the pressure rise during gas and liquid injection.

2. Method

We use the *CMG STARS* foam model, specifically the "foam interpolation model" in *STARS*, one of the most widely used mathematical representations of foam in field-scale simulations (Agada et al., 2015; AlMaqbali et al., 2015; Mukherjee et al., 2015; Sharma et al., 2017). This formulation (see Appendix A) assumes local equilibrium between the creation and destruction of lamellae as gas and surfactant solution propagate through the reservoir. Therefore, it allows performing field-scale simulations without a high computational cost. The same foam model is implemented in *CMG*'s equation-of-state simulator *GEM*. Studies show that it gives similar results to much-more-complex foam models (Cheng et al., 2000; Zeilinger et al., 1995). Our simulation parameters are based on the experimental parameters obtained by Gong et al. (2019), from steady-state data using a 17-cm-long core with a permeability (k) of 150 mD and a porosity of 0.2. The foam parameters from their study, used in the present paper, are listed in Table 1. The coreflood conditions were favorable for formation of very-strong foam. To compare the injectivity estimated by *CMG* simulations and fractional-flow-theory calculations, we use in both cases the same parameters. We neglect non-Newtonian effects and therefore do not include the foam parameters determined by Gong et al. to model non-Newtonian rheology. We assume that the region of interest is initially 100% saturated with surfactant solution.

In Fig. 1, we plot foam's apparent viscosity calculated using the parameters listed in Table 1. On the right of Fig. 1, we plot the fractional-flow curve computed using the same parameters. The large values of foam's apparent viscosity ($\approx$1 Pa s) indicate that this foam greatly reduces gas mobility. The fractional-flow curve plotted in Fig. 1 shows an abrupt drop in gas fractional flow near a water saturation around $S_w = 0.35$. This is caused by the limiting capillary pressure (Khatib et al., 1988) set at this water saturation ($fmdry = 0.35$). Also, the large value of $fmmob = 5.14 \times 10^4$ indicates a large maximum gas-mobility reduction. To compare the simulations and the calculation, we used the same gas and water viscosities (μ_{gas} and μ_{water}) presented in Table 1. These viscosities apply at the pressure (60 000 kPa) and temperature (25 °C) at which the simulations were conducted. To implement the *STARS* calculations, we construct the reservoir model illustrated in Fig. 2. The model is a square (100 $\times$ 100 m) reservoir with an injection well in its center. Originally the reservoir is divided into 5 $\times$ 5 arrays of grid blocks, each of which is 20 m $\times$ 20 m. All the grid blocks are 10 m thick. Four producing wells are in the centers of the four grid blocks at the corners. There is no flow across the outer boundaries. We examine the difference between the injection-well pressure and that at the center of the next grid block on the diagonal, at a radius equal to $r_o = \sqrt{2} \times 20$ m ≈ 28.8 m from the injection well, as shown in Fig. 2. The wellbore radius (r_w) is 0.1 m. With a porosity of 20% one pore volume out to this radius is equal

Table 1
Foam parameters and gas and water viscosities used in CMG simulations and fractional-flow calculations performed in this study.

Parameter	Value
fmdry	0.35
epdry	320
fmmob	5.14×10^4
μ_{water}	1.0×10^{-3} Pa s
μ_{gas}	1.4×10^{-5} Pa s

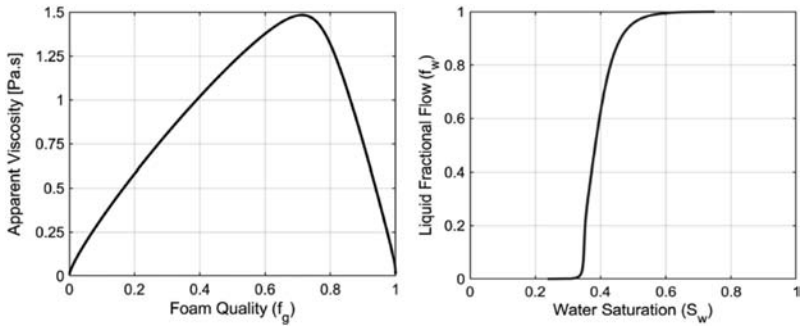


Fig. 1. On the left, plot of apparent viscosity versus gas fractional flow (f_g) (or "foam quality") computed using the parameters listed in Table 1. On the right, liquid fractional flow ($f_w = 1\text{-}f_g$) is plotted as a function of water saturation (S_w) using the same input parameters.

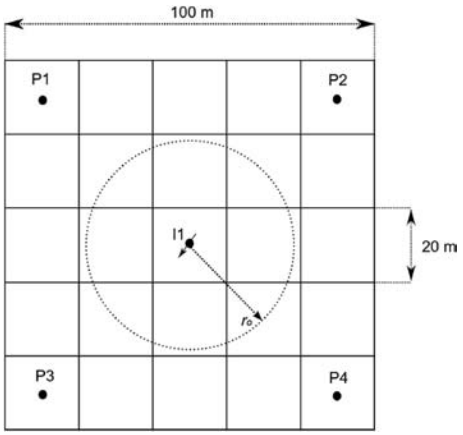


Fig. 2. Reservoir model used in simulations. ***P1***, ***P2***, ***P3,*** and ***P4*** denote four producing wells, and ***I1*** represents the injection well. In our simulations, to reduce the fluctuations caused by subdividing the central grid block, we record the difference in pressure between the injection well and the center of the next grid block along the diagonal. For fractional-flow calculations, the outer radius is taken as $r_o = \sqrt{2} \times 20\ m \approx 28.8\ m$.

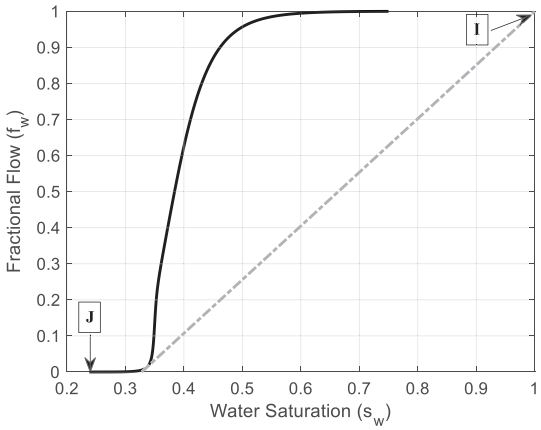


Fig. 4. Fractional-flow solution for injection of the first gas slug. Initial condition *I* and injection *J* correspond to 100% liquid saturation and 100% gas fractional flow, respectively. The dashed line represents the shock.

to 5025 m^3 in both our simulations and *FFT* calculations. In the remainder of this paper, *pore volume* refers to this volume.

The grid of this reservoir model is then refined, as illustrated in Fig. 3. This refinement is done by subdividing the nine central grid blocks into 3, 5, and 7 grid blocks. In this way, the central grid block is subdivided into 9, 25, and 49 square grid blocks, 6.7 m, 4 m, and 2.85 m on a side, respectively.

We measure injectivity in terms of dimensionless well pressure. As in our previous fractional-flow-theory calculations (*e.g.*, Al Ayesh et al., 2017), we define the dimensionless pressure (P_D) as the pressure rise caused by the presence of foam during gas or liquid injection (ΔP_{foam}) divided by the pressure rise caused by water injection into a fully water-saturated reservoir (ΔP_{liquid}) at the same volumetric rate Q:

$$P_D = \frac{\Delta P_{foam}}{\Delta P_{liquid}} \qquad \text{Eq. 1}$$

In our STARS simulations, to allow for gas compressibility, we compute injectivity using the following expression:

$$P_D = \frac{(P_{well} - P_{or})_{foam}}{(P_{well} - P_{or})_{liquid}} \frac{Q_{liquid}}{Q_{foam}} \qquad \text{Eq. 2}$$

where $(P_{well}\text{-}P_{or})_{foam}$ and $(P_{well}\text{-}P_{or})_{liquid}$ denote the pressure

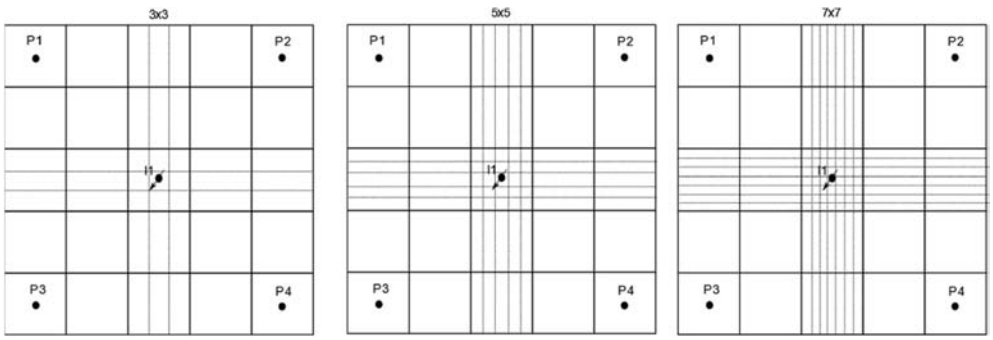


Fig. 3. Refined reservoir models used in simulations.

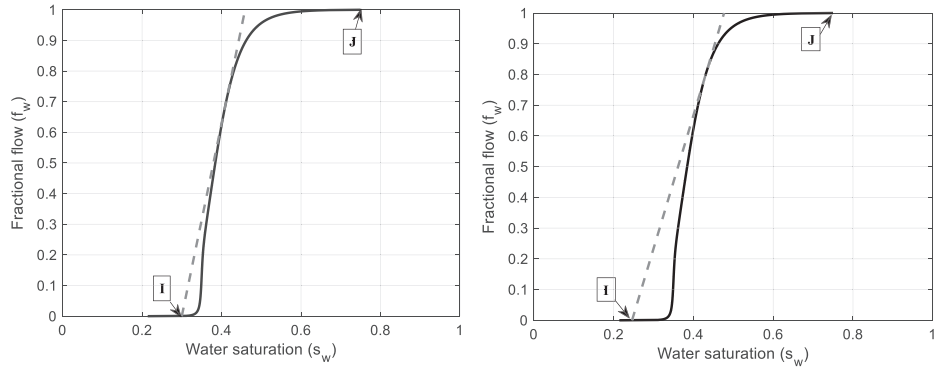


Fig. 5. Fractional-flow solutions for injection of a liquid slug after gas injection, assuming two initial water saturations S_{wI} of 0.3341 and 0.2421 in the near-well region. The slopes of the dashed lines represent the dimensionless velocities of the shocks.

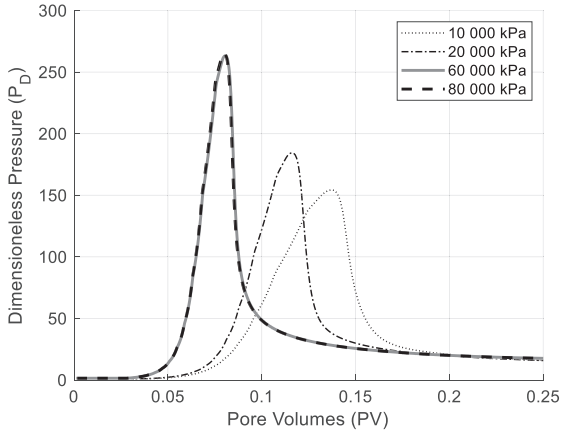


Fig. 6. Effect of reservoir pressure on the estimated injectivity during gas injection in a fully surfactant-saturated reservoir: *STARS* simulation with the base-case grid.

difference measured during foam and water injection, respectively. P_{well} corresponds to the pressure in the injection well, and P_{or} to the pressure rise in the grid block whose center coincides with the outer radius r_o (Fig. 2); Q_{liquid} and Q_{foam} denote the volumetric injection rates during water injection into a fully water-saturated formation and liquid or gas injection in SAG, respectively.

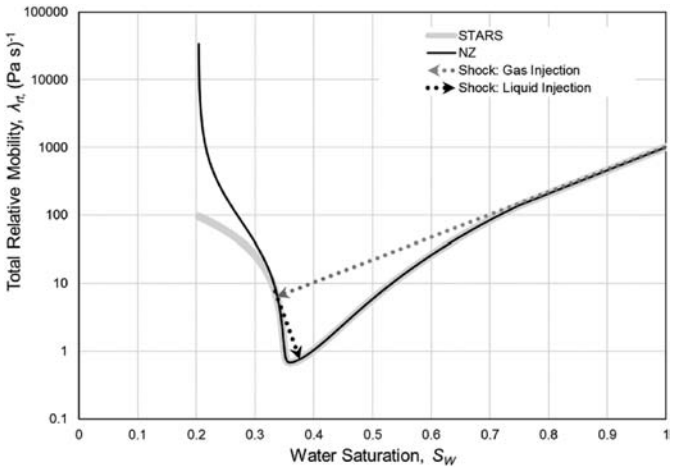


Fig. 7. Total relative mobility (λ_{rt}) of foam for the *STARS* model and considering the *NZ* correction.

Given the fluctuations in P_D caused by foam propagation through the mesh, we compute an average dimensionless pressure to compare overall injectivity during gas and liquid injections in the simulations and fractional-flow theory calculations. The average dimensionless pressure is computed using the following approximation,

$$P_{D\,avg} = \int_0^1 P_D\, dt_D \approx \sum_0^N P_D\, \Delta t_D \qquad \text{Eq. 3}$$

where $P_{D\ avg}$, P_D, t_D, and N denote the average dimensionless pressure, the instantaneous dimensionless pressure, the dimensionless time increment, and the total number of increments in dimensionless time, respectively. If all cases employed the same injection pressure (*e.g.*, if injection pressure were limiting), then the time to inject the given volume of gas or liquid would be proportional to the value of $P_{D\ avg}$.

Fractional-flow theory (*FFT*) (Buckley and Leverett, 1942) has been applied to many *EOR* processes, such as gas, polymer, surfactant, and low-salinity water flooding (*e.g.*, Pope, 1980; Walsh and Lake, 1989; Noh et al., 2007; Lake et al., 2014; Schmid et al., 2016, Luo et al., 2017, Kazemi Nia Korrani and Jerauld, 2022; Wu et al., 2023). *FFT* has reproduced key behavior during foam displacements in porous media with and without considering the presence of oil (*e.g.*, Zhou and Rossen, 1995; Mayberry et al., 2008; Dholkawala et al., 2007; Ashoori et al., 2010; Tang et al., 2019; Chengjun et al., 2022; Salazar Castillo and Rossen, 2020). To implement this model, several simplifying assumptions are made: incompressible fluids, immediate attainment to local equilibrium, one-dimensional flow, and Newtonian rheology. With these simplifying assumptions, *FFT* can provide an exact estimation of injectivity at virtually infinite grid refinement in a cylindrical reservoir model if we assume that the foam model is a complete description of foam behavior.

3. Calculation

We implement fractional-flow theory in a radial-flow model with a wellbore radius r_w equal to 0.1 m and outer radius r_o equal to 28.8 m to mimic the reservoir model created in the simulator (Fig. 2). We use an updated version of a Matlab code already implemented to model foam diversion between different-permeability layers (Al Ayesh et al., 2017) and injectivity during gas injection in a SAG process (Salazar Castillo and Rossen, 2020). The first gas slug is injected into a fully surfactant-saturated

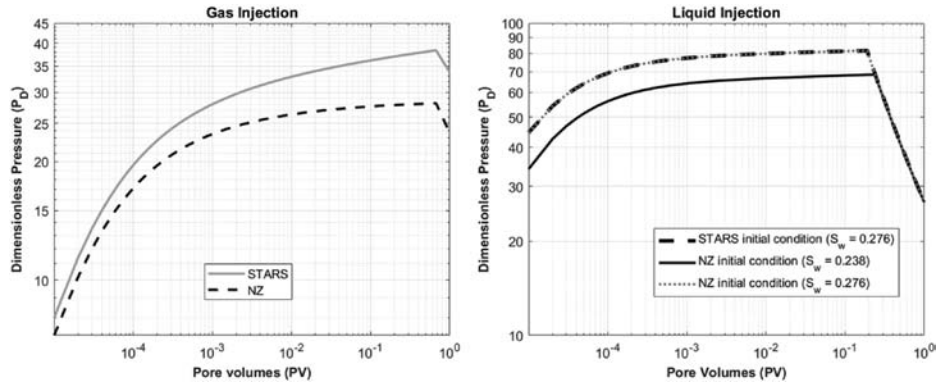


Fig. 8. Fractional-flow-theory calculations of gas and liquid injectivities. On the left, dimensionless pressure (P_D) during the injection of the first gas slug. On the right, P_D during the injection of the subsequent liquid slug.

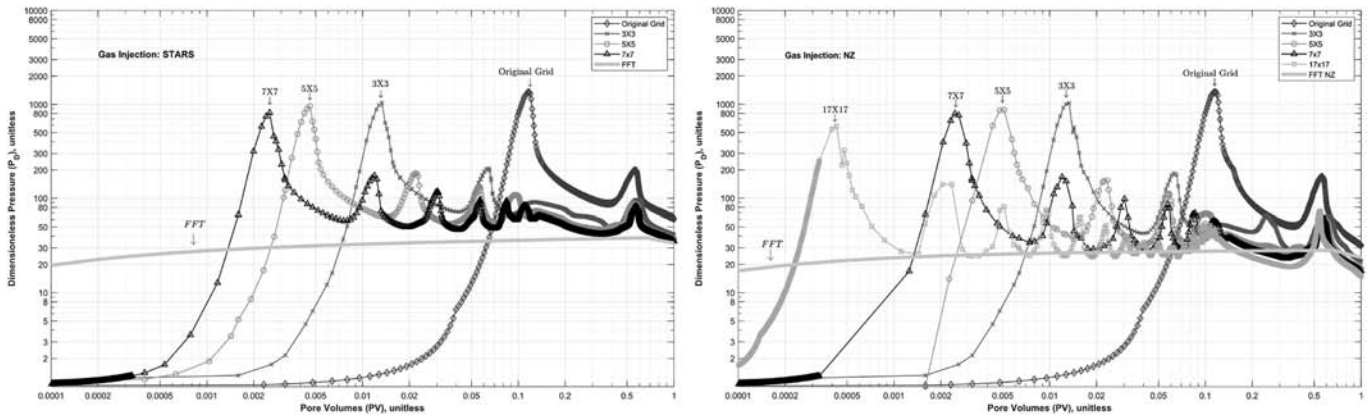


Fig. 9. Gas injectivity at early times for the original reservoir model and the three refined-grid cases (3×3, 5×5, and 7×7)) for the one that includes the STARS model but excludes the NZ correction (top plot) and four refined cases (3×3, 5×5, 7×7 and 17×17) for the scenario that includes the *NZ* correction (bottom plot). In these results, we use the injection-well pressure calculated using the Peaceman model implemented in STARS. To compare, we also plot the results of our *FFT* calculations excluding or including the *NZ* correction.

reservoir. Therefore, in our *FFT* code, the initial uniform condition corresponds to 100% water saturation, while the injection condition corresponds to a water saturation at irreducible water saturation. Fig. 4 shows the fractional-flow solution corresponding to these initial (I) and boundary (J) conditions.

At the end of gas injection, there is a range of saturations in the reservoir in both the *CMG* simulations or in the *FFT* calculations. According to *FFT*, upon water injection into a reservoir with a water saturation increasing downstream, the shock will accelerate, creating a complex scenario. It is possible to greatly simplify the modelling of liquid injection using *FFT* by assuming a uniform water saturation. For simplicity, we make this assumption. We selected the initial water saturation so that its value will reproduce the injectivity (or mobility) found in the reservoir at the end of the gas-injection period. Fig. 5 illustrates the shock construction for two cases with different initial water saturations ($S_w = 0.2421$ and $S_w = 0.3341$). As the water saturation of the initial condition increases, the shock velocity also increases. Water saturation in the vicinity of the well at the end of gas injection varies in a region between these two values (Appendix B, Fig. B.1).

The simulations were performed using the same foam parameters as our *FFT* calculations (Table 1). Additionally, we specify the relative-permeability parameters (See Appendix A) using Stone's Model II for three phases (gas, water, and oil). For simplicity, we assume that no oil is present from the beginning of our simulations. For all the simulations, the injections were set to 3.2 pore volumes (PV) of gas followed by 3.2 PV of liquid, so that the entire reservoir model would be completely swept by the injected fluid. Fractional-flow calculations for foam displacements neglect gas compressibility, whereas simulations allow gas expansion. To reconcile the two approaches, we raised the reservoir pressure in our simulations to minimize the effect of gas compressibility on estimated injectivity. To this end, we set the reservoir pressure to 60 000 kPa. According to our simulations, at this value of initial reservoir pressure, injectivity during gas injection in a fully surfactant-saturated reservoir is affected only slightly by gas expansion, as illustrated in Fig. 6. To illustrate this, consider a reservoir pressure and temperature set to 60 000 kPa and 25 °C, respectively, and a maximum pressure of 61062 kPa, as in our simulations. At these values of pressure, the minimum and maximum nitrogen density (according to Redlich and Kwong (1949) equation of state used in the simulator) is 478.5 and 483.5 kg/m^3, respectively. This translates into a variation of gas density of less than 1%, making nitrogen compressibility negligible.

A crucial issue is whether foam collapses completely as it dries out in the near-well region during gas injection. If it does, it is possible to model this complete foam collapse at irreducible water saturation S_{wr} by incorporating the *NZ* correction to the *STARS* foam model (Namdar Zanganeh et al., 2014), as described in Appendix A. In Fig. 7, we illustrate the total relative mobility (λ_{rt}) of foam as a function of water saturation for the *STARS* foam model

and for the *STARS* foam model including the *NZ* correction. Since the *NZ* correction does not affect the fitting of the foam parameters in a *SAG* process (Salazar Castillo and Rossen, 2020), both curves were computed using the parameters of Table 1. One observes that including the correction dramatically increases the mobility at and near S_{wr}. This behavior is key for injectivity during gas injection in a *SAG* process. We include this correction in our *STARS* simulations and fractional-flow-theory calculations to study the impact of foam collapse at S_{wr} on injectivity.

4. Results

4.1. Fractional-flow theory (FFT) calculations

Gas and liquid injectivities as predicted by *FFT* are presented in Fig. 8. We show two estimates of gas injectivity, one employing the original *STARS* foam model and the second including the *NZ* correction. Gas injectivity is greatly affected by the incorporation of the *NZ* correction, which reduces the peak dimensionless pressure by ten units. In contrast, with the same initial condition liquid injectivity is not significantly affected by the *NZ* correction. Instead, liquid injectivity is affected by the initial condition representing foam presence after gas injection. The drier the initial state, the better is injectivity during liquid injection (Fig. 8, right, and Appendix B, Fig. B.2). The duration of the plateau in P_D during liquid injection in Fig. 8 reflects the velocity of the shock (Fig. 5). As noted above, to estimate injectivity in our *FFT* calculations, we assumed two cases with uniform initial water saturations $S_w = 0.276$ and $S_w = 0.238$. These saturations correspond to an initial $P_D = 24.75$ and an initial $P_D = 14.75$, at the end of the gas injection period (3.2 *PV*), for the *FFT* calculations using the original *STARS* model and the *NZ* correction, respectively. We present the dimensionless time-distance diagrams corresponding to our liquid and gas *FFT* calculations in Appendix B, and in Appendix C a summary of liquid's and gas' time-average injectivity as average dimensionless pressure ($P_{D\ avg}$) obtained in simulations and the *FFT* calculations.

4.2. Comparison between conventional simulations (including the Peaceman model) and fractional-flow-theory calculations

In Fig. 9 we present the behavior of the dimensionless pressure P_D during the injection of the first gas slug as estimated by *FFT* and *CMG's* simulations for the *STARS* model (on the top graph) and with the *NZ* modification (on the bottom graph). Time is on a logarithmic scale to emphasize the complex dynamics at early times. The pressure peak in all the simulations is consistently higher than the maximum dimensionless pressure P_D calculated using fractional-flow theory, even when including the *NZ* correction.

In the simulations, it takes some time for gas to accumulate and reduce mobility (Fig. 7) in a large grid block. Therefore, the peak in P_D occurs later as the grid block size increases. In *FFT*, the shock to a low-mobility foam state occupies the region immediately around the well quickly, with a large effect on injectivity. Then, in our simulations, secondary peaks in P_D smaller in magnitude than that of the first peak take place. The number of secondary peaks increases as the grid is refined reflecting the effect of foam creation on subsequent grid blocks as gas propagates outward. These fluctuations are an effect of the mesh and cannot be eliminated.

The 7×7 grid refinement reduces the average dimensionless pressure $P_{D\ avg}$ from 133 to 51 (Appendix C; Table C.1) in the simulations that exclude the *NZ* correction. However, it still exceeds the *FFT* $P_{D\ avg}$ of 37, which implies an error of 38%. Fig. 10 plots the value of $P_{D\ ave}$ vs. the size of the injection-well grid block in the case of the Peaceman model, no *NZ* correction or other adjustment, for gas injection. The fit to the $P_{D\ ave}$ indicates that for achieving the *FFT* estimate of average injectivity, one would require a grid refinement of the injection well grid block of more than 571 divisions with a well grid block with a length of about 3.5 cm. To our knowledge this level of resolution is not used in any simulation study at the field scale. The trend also suggests that $P_{D\ avg}$ would still be over 40 for a grid-block size of 0.61 m as in the study of Mukherjee et al. (2015).

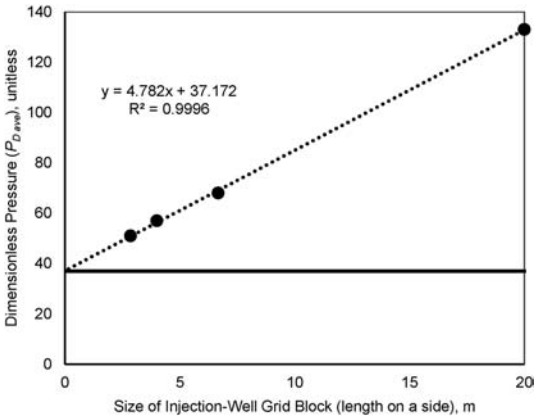


Fig. 10. Value of $P_{D\ ave}$ as a function of size of the injection-well grid block for the case of Peaceman model, no *NZ* or other modification. Black dots: simulation results. Dashed line fit to simulation results. Black line, *FFT* result.

Fig. 11 plots the time of occurrence of the first P_D peak for the gas injection case when excluding the *NZ* correction. This time is reduced as we refined the grid with a trend that goes as the square of the length of the well grid block (L^2). If the length of the well grid block (L) tends to zero, the appearance of the first pressure rise would occur immediately, as in the *FFT* calculation. The L^2 trend corresponds to the volume of the well grid block that has a fixed height of 10 m. P_D behavior during gas injection when including the *NZ* correction is like that observed without the correction. However, P_D is smaller at gas breakthrough (about 0.7 *PV*) in all the simulations (3×3, 5×5, 7×7, and 17×17) than the *FFT* estimate at the same dimensionless time. Moreover, the *NZ* correction has a large impact on $P_{D\ avg}$ (Appendix C), with a value of 26 in the 17×17 refined case, implying an error of less than 4% when compared with the *FFT* calculation. Nevertheless, this grid resolution increased the computation time 30 times and is not expected to be used in

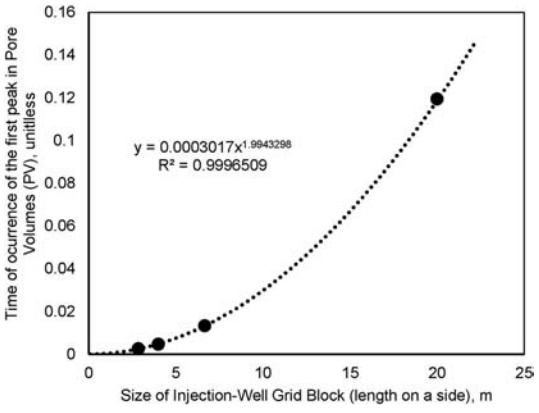


Fig. 11. Time of occurrence of the first dimensionless pressure peak as a function of size of the injection-well grid block for the case of Peaceman model, no *NZ* or other modification. Black dots: simulation results. Dashed line fit to simulation results.

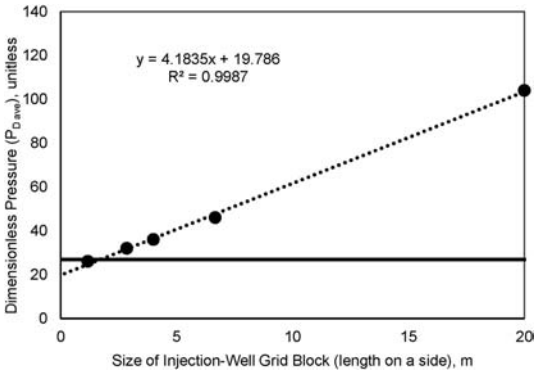


Fig. 12. Value of PD_{ave} as a function of size of the injection-well grid block for the case of Peaceman model, including *NZ* correction. Black dots: simulation results. Dashed line fit to simulation results. Black line, FFT result.

routine simulations. Moreover, simulation using the NZ correction does not converge to the FFT solution with infinite grid resolution. The best degree of grid refinement would likely vary with foams of different strengths and other variations in conditions.

Fig. 12 plots the value of $P_{D\,ave}$ vs. the size of the injection-well grid block in the case of the Peaceman model, including the *NZ* correction, for gas injection. The fit to the $P_{D\,ave}$ indicates that for achieving the *FFT* estimate of average injectivity, one would require a grid refinement of the injection well grid block of about 17 blocks with a length of about 1.18 m each. We included a calculation using this level of resolution (Fig. 9) to test if $P_{D\,ave}$ can match the fractional-flow theory. As pointed out above, this level of resolution (17×17) resulted in an error of less than 4%. Liquid-injectivity estimates as predicted by *FFT* and the simulations are presented in Fig. 13. In the top graph we present the results that neglect the *NZ* correction and in the bottom graph the results that include it. In all cases, liquid injection begins after 3.2 *PV* of gas

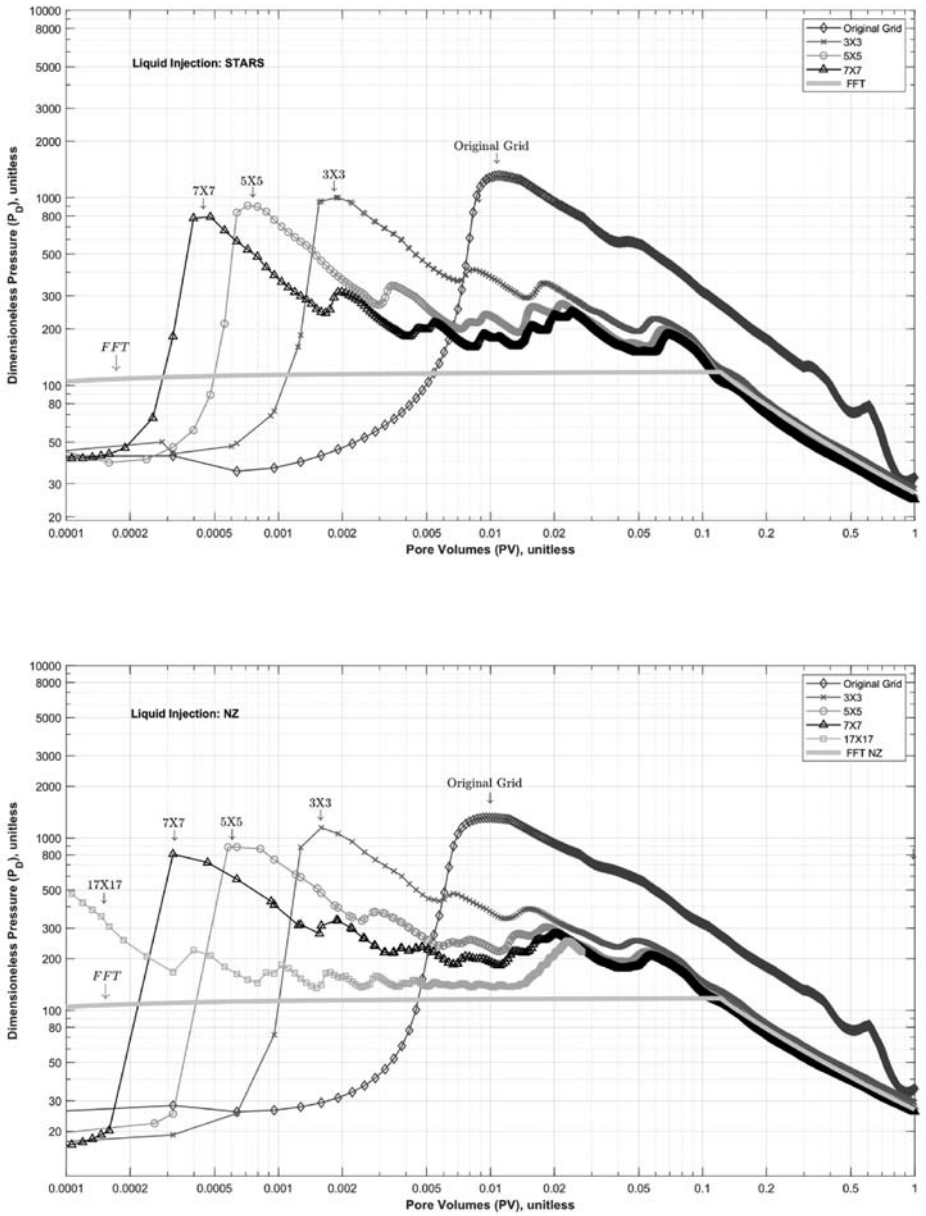


Fig. 13. Fractional-flow theory (*FFT*) calculations and *STARS* simulations of liquid injectivity at early times using the Peaceman model as implemented in the simulations. On the top plot we exclude the *NZ* correction, while on the bottom plot we include the *NZ* correction.

injected. Given that foam is already present in the reservoir, the pressure peaks in the simulations during liquid injections occur earlier than during gas injection. Liquid saturates the smaller grid blocks faster, resulting on peaks occurring at an even earlier time. The magnitudes of these peaks are consistently larger than the maximum pressure rise predicted by *FFT*.

The *NZ* correction alters the final water-saturation distribution along the reservoir at the end of gas injection. This causes slightly different initial P_D in both the *FFT* calculations and the simulations. In the liquid injectivity simulations, the initial P_D is about 40 when neglecting the *NZ* correction and about 20 when including it (Fig. 10). However, the impact of these different initial conditions on $P_{D\ avg}$ is modest during liquid injection (Appendix C). The variations caused by the *NZ* correction on $P_{D\ avg}$ are at most 5% during liquid injection. In contrast, during gas injection the *NZ* correction causes a variation of at least 28%. Therefore, the *NZ* correction does not alter significantly the average injectivity during liquid injection, as is also observed in the *FFT* calculations (Appendix C). The minimum error (7×7 refinement) in simulated $P_{D\ avg}$ during liquid injection is 16% when excluding the *NZ* correction and 21% when including it at 17×17 refinement in this last case.

4.3. Comparison between simulations that exclude the Peaceman model and fractional-flow-theory calculations

Injectivity in radial flow depends strongly on mobilities very near the wellbore. Therefore, the Peaceman model, which applies the average saturation of the grid block to the near-wellbore region, could introduce a larger error in the calculated injectivity in the presence of foam. To test the impact of the Peaceman model on injectivity, we redo our simulations excluding it (Sharma et al., 2017); we equate the pressure of the center grid block with that at the well during foam injection to estimate injectivity in the refined-grid cases. However, we keep the reference pressure rise caused by water injection into a fully water-saturated reservoir (ΔP_{liquid}) as predicted when including the Peaceman model to calculate the dimensionless pressure (Eq. (1)). For illustration purposes, we perform this test excluding the *NZ* correction, which primarily affects the central grid block. Similar conclusions can be reached including the *NZ* correction, which has a significant effect only at low water saturations very near the wellbore during gas injection (Fig. 7; Appendix B, Fig. B.1).

When excluding the Peaceman model, the peak in P_D occurs earlier and its magnitude increases as we refine the grid for the gas and liquid injection periods (Figs. 14 and 15) as in the simulations that include it. We observe that the P_D behavior of the 7×7 simulation that excludes the Peaceman model is practically the same as the 7×7 simulation that includes it (Figs. 9 and 10). In fact, $P_{D\ avg}$ is 51 during gas injection and 57 during liquid injection for both 7×7 cases (Appendix C). Therefore, the effect of excluding the Peaceman model on P_D is practically eliminated when the grid is refined to a 7×7 resolution. The procedure that excludes the Peaceman model gives better estimates of liquid and gas average injectivities without requiring extraordinary grid refinement (Appendix C). The calculation of $P_{D\ avg}$ indicates that the error is 29.7% for gas injection and 12.2% for liquid injection in the 3×3 refined grid case when excluding the Peaceman model. On the other hand, when including the Peaceman model the error in $P_{D\ avg}$ is 38% for gas injection and 16% for liquid injection in the 7×7 refined grid case. Fig. 16 plots the value of $P_{D\ ave}$ vs. the size of the injection-well grid block in the case that excludes the Peaceman model, and excluding the NZ correction, for gas injection. The fit to the $P_{D\ ave}$ indicates that simulations excluding the Peaceman model do not match exactly the *FFT* estimate of average injectivity at any resolution. However, the error is reduced significantly and the error at coarser grids is less significant than in the cases that include the Peaceman equation.

4.4. Comparison between simulations that neglect foam presence in the central grid block and fractional-flow-theory calculations

Since it is not possible to reconcile the estimates of gas and liquid injectivities obtained through *FFT* calculations and *STARS* simulations, even when neglecting the Peaceman model or including the *NZ* correction, we tested an additional procedure: disallowing foam presence in the central grid block while including the Peaceman equation (Sharma, 2019; Sharma et al., 2017). Disallowing foam there does not correct or modify the model; it simply neglects foam presence in that grid block, to improve injectivity using a practical approach and has no physical basis. Neglecting foam presence can be done by setting *fmmob* equal to zero in the central grid block (Appendix A). These simulations were performed only for the refined-grid cases (3×3, 5×5 and 7×7). We compare the results of the *STARS* simulations obtained by following this

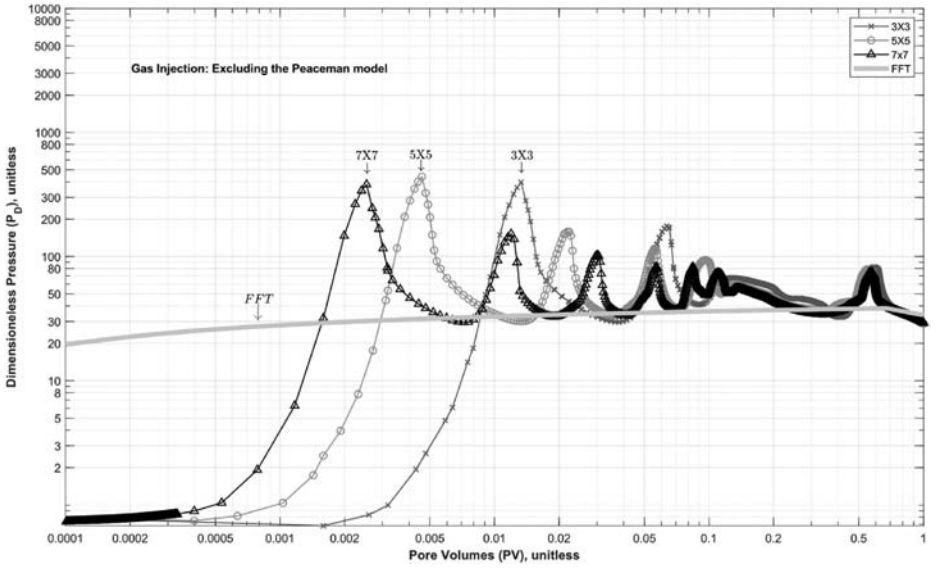


Fig. 14. Fractional-flow-theory calculations and simulations of gas injectivity obtained excluding both the Peaceman model and the *NZ* correction.

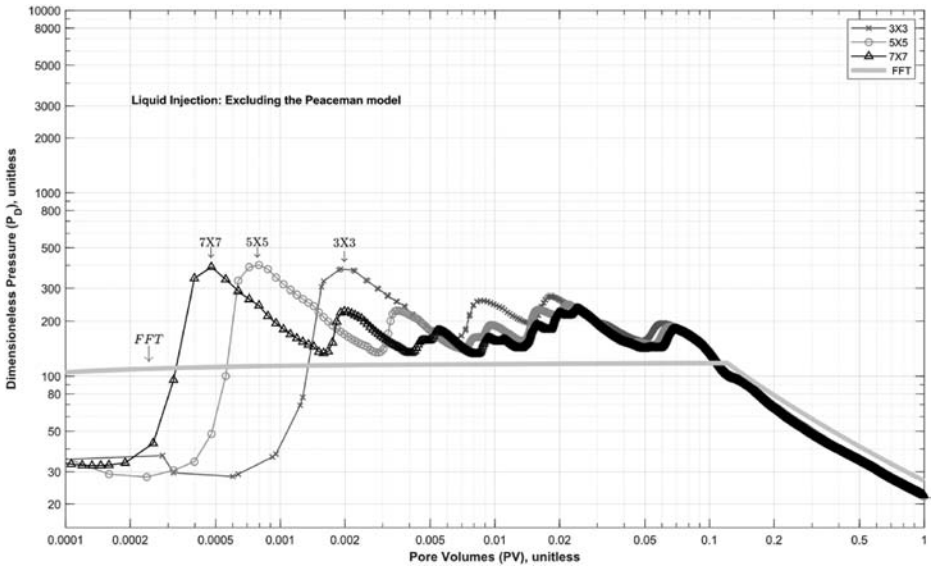


Fig. 15. Fractional-flow theory calculation and *STARS* simulations of liquid injectivity calculated excluding the Peaceman model. These cases also exclude the *NZ* correction.

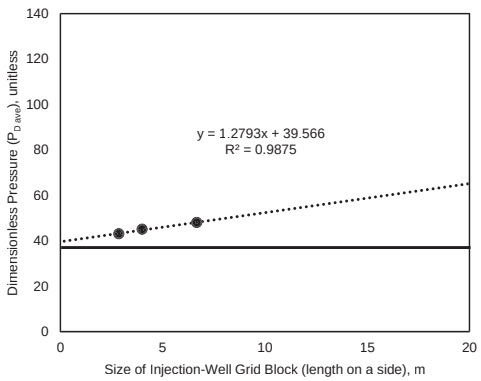


Fig. 16. Value of PD_{ave} as a function of size of the injection-well grid block for the case that excludes both the Peaceman model and NZ correction. Black dots: simulation results. Dashed line fit to simulation results. Grey line, FFT result.

procedure against our *FFT* calculations performed including the *NZ* correction, since this correction assumes foam collapse at S_{wr}.

For gas injection (Fig. 17), in each simulation case, there is a first peak in P_D that corresponds to gas accumulation (without foam creation) in the central grid block. The magnitudes of these peaks are modest (no more than $P_D = 5$) indicating mobility reduction by gas presence. They occur earlier and reduce their magnitude as we refine the grid. Then, secondary peaks appear once foam is created as gas travels to the next grid blocks, reducing mobility greatly. Compared to the previous simulation cases (including foam in the central grid block) the maximum mobility reduction takes longer to appear, which is expected since foam is created away from the injection-well grid block. The average dimensionless pressure $P_{D\,avg}$ is 38 for the 3×3 case, implying an error of 40.7% compared to the *FFT* calculation that incorporates the *NZ* correction ($P_{D\,avg}$ of 27). This error is not reduced by grid refinement.

During subsequent liquid injection (Fig. 18) we observe an initial mobility increase as liquid accumulates in the central grid block.

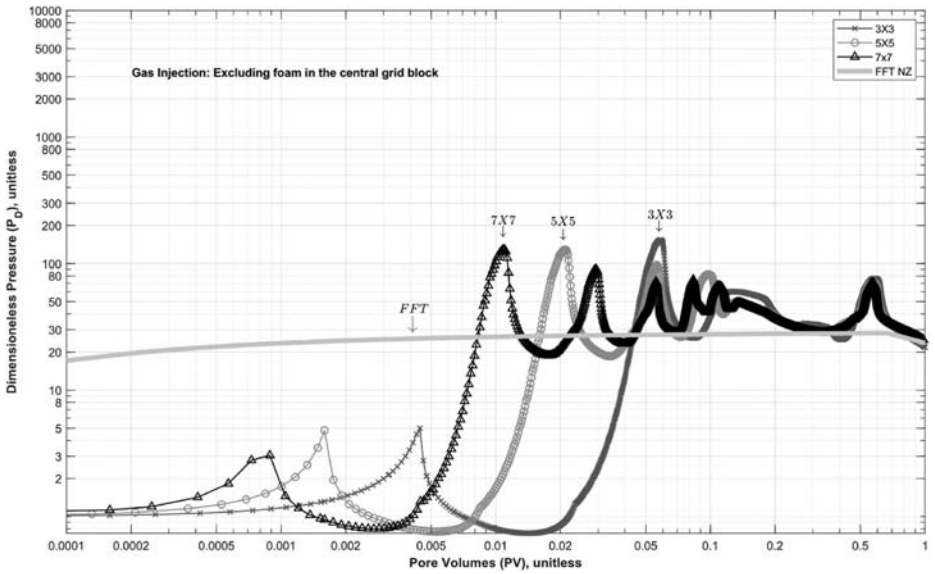


Fig. 17. Fractional-flow-theory calculation and simulations of gas injectivity at early times excluding foam in the central grid block (*fmmob* = 0).

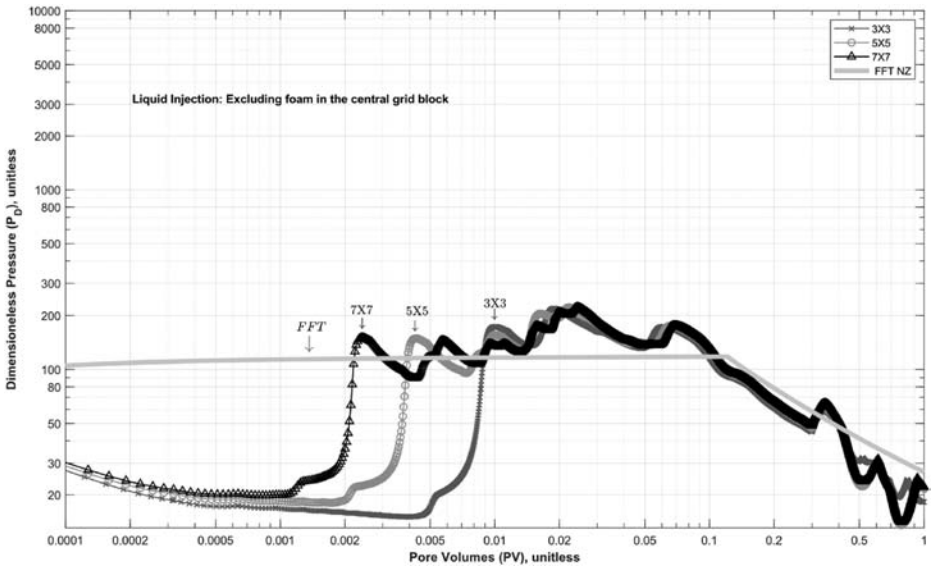


Fig. 18. Fractional-flow theory calculations and simulations of liquid injectivity at early times with foam excluded in the central grid block (*fmmob* = 0 there).

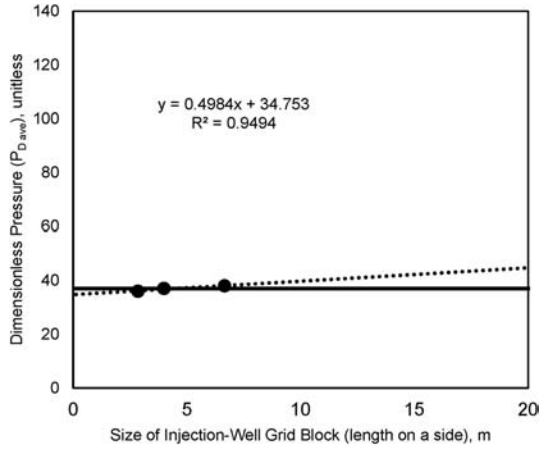


Fig. 19. Value of PD_{ave} as a function of size of the injection-well grid block for the case that excludes foam at the well grid block. Black dots: simulation results. Dashed line fit to simulation results. Black line, *FFT* result.

Later, mobility is reduced as foam is created in the next grid blocks. As in gas injection, maximum mobility reduction takes a longer time than in the cases where foam is included in the central grid block. The error in $P_{D\ avg}$ for liquid injection is 7%, the smallest of all the procedures tested in this study and without requiring grid refinement. Fig. 19 plots the value of $P_{D\ ave}$ vs. the size of the injection-well grid block in the case that excludes foam in the well grid block for gas injection. This fit indicates that it is possible to match the *FFT* estimate of average injectivity at a refinement of 4.5 on the well grid block with a grid block length of 4.4 m. This was the only strategy that achieved a match at reported grid refinement resolutions. Again, the best degree of grid refinement would likely vary with foams of different strength and other variations in conditions.

5. Discussion

Our results compare numerical simulations to fractional-flow theory assuming the foam model to be correct. We have left out a number of factors that affect injectivity and are not accounted for in the model. As noted by Gong et al. (2019, 2020a, b) evaporation of water very near the wellbore can have significant effects on both gas and subsequent water injectivity. Fingering of water through trapped gas, and dissolution of trapped gas within the fingers, is crucial to liquid injectivity and not accounted for in the model. In addition, accounting for shear-thinning foam behavior would further increase injectivity (Salazar-Castillo et al., 2019). Accounting for non-Newtonian foam behavior is possible with *FFT* but much more complex than modeling Newtonian behavior.

Our simulations show peaks in dimensionless injection pressure P_D as the central (injection-well) grid block, and then surrounding grid blocks, experience similar peaks during gas or liquid injection. The periods of peak P_D during gas injection are brief in our results, typically a few hundredths of a pore volume (Fig. 9). However, if injection pressure is fixed, the period of low injectivity is proportional to the decline in injectivity. For instance, if at fixed injection rate injectivity is reduced 5× for a time in one case compared to another, then at fixed injection pressure the time required to pass through this period is 5x greater in the first case than the second. This is reflected in the value of average dimensionless average $P_{D\ ave}$ (Eq. (3)). We have based our foam parameters on a fit to laboratory data (Gong et al., 2019) taken under conditions ideal for strong foam: room temperature; strongly water-wet, high-permeability sandstone; low salinity; absence of oil. The magnitude of injectivity reduction in field applications would be much less than that shown in our results. Moreover, reservoir heterogeneity, gravity segregation, residual oil near the well, wellbore skin effects and well stimulation would further complicate injectivity in the field. Further work is needed to quantify the quality of the fit of simulation results in such cases.

At the conditions and model that we selected to run the simulations (a few pore volumes of fluid injected, high reservoir pressure and low temperature), we cannot model evaporation, fingering and dissolution effect. Therefore, these effects must be addressed in future studies. We selected experimental data of a single foam scan for this study. A sensitivity analysis is outside the scope of our study and could be a topic for future research that must include simulations and experiments to justify the variation of the parameters in each reservoir or experimental conditions. The purpose of this study is to illustrate how grid refinement plays a role in foam flow simulations at field scale. Whether our observations hold to any other conditions and foam models that would

be the topic of future research and not possible to address in a single study.

6. Conclusions

Grid refinement in conventional foam simulations reduces the peak in injection-well pressure and causes it to drop more quickly, roughly in proportion to the volume of the injection-well grid block. Compared to the base-case grid, the initial peaks in pressure in the refined grids occur faster for both liquid and gas injection as we refine the grid. Grid refinement improves the estimation of injectivity during gas injection but does not match the prediction of fractional-flow theory using the same foam model. For liquid injectivity after injection of a modest gas slug, grid refinement at the 7×7 resolution gives a reasonable estimate of average overall injectivity.

During gas injection, incorporating the Namdar-Zanganeh (*NZ*) correction that assumes complete foam collapse at S_{wr} in the refined-grid calculations further improves estimated injectivity and reduces the difference between the injectivity calculated using fractional-flow theory and the simulations. Liquid injectivity is not significantly affected by the incorporation of the *NZ* correction, and grid refinement gives a reasonably good estimate (as without the *NZ* correction) of liquid injectivity with the 7×7 grid refinement tested at early injection times.

Excluding the Peaceman model with the procedure proposed in this study gives estimates of gas and liquid average injectivities closer to fractional-flow theory estimates, without requiring extraordinary grid refinement. This procedure has the advantage of being able to include the *NZ* correction, if needed. The procedure of excluding foam in the injection-well grid block by setting *fmmob* to zero there gives the closest estimates of gas and liquid average injectivities to fractional-flow theory without requiring extraordinary grid refinement. Moreover, this method gave the smallest error in average liquid injectivity (7%) of all the methods tested in this study. This method in effect already includes the *NZ* correction.

Research is ongoing on methods to extend grid refinement in practical reservoir simulation. This work shows the need for extended grid refinement for accurate prediction of foam injectivity in SAG applications.

Terms and abbreviations

EOR	Enhanced Oil Recovery
epdry	Parameter in the STARS foam model controlling the abruptness of foam collapse at the limiting liquid saturation, unitless
FFT	fractional-flow theory
F_2	Dry-out function
f_g	Gas fractional flow, unitless
f_w	Water fractional flow, unitless
FM	Mobility-reduction factor, unitless
fmdry	Limiting liquid saturation in the STARS foam model, unitless
fmmob	Reference gas-mobility-reduction factor in the STARS foam model, unitless
I	Initial condition in fractional-flow theory calculation, unitless
J	Injection condition in fractional-flow theory calculation, unitless
k	Permeability, mD
k_{rg}	Gas relative permeability, unitless
k_{rg}^f	Gas relative permeability in the presence of foam, unitless
k_{rw}	Water relative permeability, unitless
k_{rw}^0	End-point water relative permeability (Eq. (A.1), unitless
k_{rg}^0	End-point gas relative permeability (Eq. (A.2), unitless
KROCW	End-point oil relative permeability at connate water in STARS, unitless
KRWIRO	k_{rw}^0 in STARS, unitless
KRGCL	End-point gas relative permeability at the connate liquid in STARS, unitless
KROGCG	k_{rg}^0 in STARS, unitless
λ_{rt}	Total relative mobility, $(\text{Pa s})^{-1}$
μ_{app}	Foam apparent viscosity, Pa s
μ_g	Gas viscosity, Pa s
μ_w	Water viscosity, Pa s
n_g	Gas Corey-Brooks exponent (Eq. (A.2), unitless
Ng	n_g exponent in *STARS*, unitless
n_w	Water Corey-Brooks exponent (Eq. (A.1), unitless
Nw	n_w exponent in *STARS*, unitless
NZ	Namdar-Zanganeh correction
P_D	Dimensionless pressure, unitless
P_w	Pressure at the injection well, Pa
P_{ro}	Pressure in the grid block whose center coincides with the radius 28.8 m (Fig. 2), Pa
∇P	Pressure gradient, Pa
ΔP_{foam}	Pressure difference during liquid or gas injection in the presence of foam, Pa
ΔP_{liquid}	Pressure difference during liquid injection in the absence of foam, Pa
PV	Pore volumes injected, unitless
Q	Volumetric flow rate, m^3/s
Q_{foam}	Volumetric flow rate for liquid or gas injection in the presence of foam, m^3/s
Q_{liquid}	Volumetric flow rate for liquid injection in the absence of foam, m^3/s
r_o	Outer radius (Fig. 2), m
r_w	Wellbore reservoir radius, m
S	Normalized water saturation, unitless
SAG	Surfactant Alternating Gas
SFBET	*epdry* in *STARS*, unitless
SFDRY	*fmdry* in *STARS*, unitless
S_g	Residual gas saturation, unitless
SGCON	Connate gas saturation in *STARS*, unitless
SGCRIT	Critical gas saturation in *STARS*, unitless
S_{gr}	Residual gas saturation, unitless
S_o	Oil saturation, unitless
SOIRW	Irreducible oil saturation for water-oil table in *STARS*, unitless
SORW	Residual oil saturation for water-oil table in *STARS*, unitless
SOIRG	Irreducible oil saturation for gas-liquid table in *STARS*, unitless
SORG	Residual oil saturation for gas-liquid table in *STARS*, unitless
S_w	Water saturation, unitless
S_{wr}	Residual water saturation, unitless
SWCON	Connate water saturation in STARS, unitless
SWCRIT	Critical water saturation in STARS, unitless
U_g	Gas superficial velocity, m/s
U_t	Total superficial velocity, m/s
U_w	Water superficial velocity, m/s

CRediT authorship contribution statement

Rodrigo O. Salazar Castillo: Writing – review & editing, Writing – original draft, Validation, Software, Methodology, Investigation, Formal analysis, Data curation, Conceptualization. **Lily Qian:** Writing – review & editing, Visualization, Software, Data curation. **Bibiana Téllez García:** Writing – review & editing, Visualization, Software, Data curation. **William R. Rossen:** Writing – review & editing, Writing – original draft, Supervision, Project administration, Methodology, Funding acquisition, Conceptualization.

Declaration of competing interest

The authors declare that they have no known competing financial interests or personal relationships that could have appeared to influence the work reported in this paper.

Acknowledgements

This project was supported by the Joint Industry Project (*JIP*) on Foam for EOR at the Delft University of Technology (*TU Delft*). We thank and acknowledge both the sponsorship and advice of sponsoring companies and their representatives. We thank Gemma Jones and Fabiola Vivas of the Computer Modelling Group for his valuable advice on the *CMG* simulations performed in this paper. Rodrigo Salazar thanks *TU Delft* for the facilities provided and the Mexican Institute of Petroleum for the support during his Ph.D. studies. Bibiana Téllez thanks *CONAHCYT (now SECIHTI)* for the scholarship provided during her Ph.D. studies and *INAOE* for the support during the development of this project.

APPENDIX A. Relative-Permeability Model and Foam Model

In the fractional-flow theory calculations, we used the Corey-Brooks relative-permeability models for water and gas relative permeabilities, which are defined by

$$k_{rw} = k^0_{rw} S^{n_w} \tag{A.1}$$

$$k_{rg} = k^0_{rg} (1 - S)^{n_g} \tag{A.2}$$

$$S \equiv \frac{S_w - S_{wr}}{1 - S_{wr} - S_{gr}} \tag{A.3}$$

where k_{rw}, k_{rg}, k^0_{rw}, k^0_{rg}, n_w, n_g, S, S_w, S_{wr} and S_{gr} denote, respectively, liquid and gas relative permeabilities, the end-point water and gas relative permeabilities, the water and gas Corey-Brooks exponents, normalized water saturation, water saturation, and the residual water and gas saturations.

In Table A.1, we list the Corey-Brooks parameters used in this study. These parameters were fitted by Gong et al. (2019) to their coreflood data.

Table A.1
Corey-Brooks parameters and foam parameters used in the fractional-flow calculations performed in this study.

Relative permeability function parameters (Gong et al., 2019)	
$S_{wr} = 0.204$	$S_{gr} = 0.25$
$k^0_{rw} = 0.14$	$k^0_{rg} = 0.47$
$n_w = 5.25$	$n_g = 1.22$

The STARS simulator assumes three-phase flow: gas, water, and oil. The relative permeabilities of these phases are represented using the modified Stone's Model II. In this model, the three-phase water relative permeability is a function of water saturation S_w (Eq. (A.1) and is equal to that of the two-phase system consisting of water and oil. The three-phase gas relative permeability is a function of gas saturation S_g (Eq. (A.2) and is equal to that of the two-phase system consisting of water and gas. The three-phase oil relative permeability is calculated using the modification of Aziz and Settari (1979).

Since we perform our simulations in the absence of oil ($S_o = 0$), the three-phase gas relative permeabilities effectively correspond to the Corey-Brooks two-phase relative permeabilities used in the fractional-flow calculations. Therefore, we assigned in the simulator arbitrary values to the parameters controlling oil mobilities and the Corey-Brooke values of Table A.1 to the parameters controlling gas and liquid mobilities, as listed in Table A.2. In the presence of foam, the STARS model (Computer Modelling Group Ltd, 2016; Cheng et al., 2000) represents the effect of foam by altering the gas relative permeability (e.g., Eftekhari and Farajzadeh, 2017). To model this effect, it applies a mobility-reduction factor, *FM*, to the gas phase as follows

$$U_t f_g = -\frac{k\, k^f_{rg}}{\mu_g} \nabla P = -\frac{k\, k_{rg}\, FM}{\mu_g} \nabla P \tag{A.4}$$

where U_t, f_g, k, k_{rg}, k^f_{rg}, μ_g and ∇P denote, respectively, total superficial velocity, foam quality (gas fractional flow), permeability, gas relative permeability in the absence and presence of foam, respectively, gas viscosity and pressure gradient.

The mobility-reduction factor, *FM*, models the effects of surfactant concentration, water saturation, oil saturation, gas velocity, capillary number, and the critical capillary number, respectively, on gas mobility. Here we focus on the dependence on water saturation (and, by implication, on capillary pressure) through the function F_2, which controls behavior in the high-quality regime:

$$FM = \frac{1}{1 + fmmob\, F_2} \tag{A.5}$$

where the parameter *fmmob* is the reference (maximum) gas-mobility-reduction factor for wet foams.

F_2, also known as the dry-out function, models the abrupt collapse of foam produced by the limiting capillary pressure (Khatib et al., 1988) at a characteristic water saturation value (*fmdry* in STARS) with the following expression:

$$F_2 = \left[0.5 + \frac{\arctan\left(epdry(S_w - fmdry)\right)}{\pi}\right] \tag{A.6}$$

where *epdry* controls the abruptness of the transition. This model does not incorporate complete foam collapse at irreducible water saturation, S_{wr}. To reflect complete foam collapse at S_{wr}, we add the NZ modification (Namdar Zanganeh et al., 2014). In this case, the expression for F_2 is

$$F_2 = \left[0.5 + \frac{\arctan\left(epdry(S_w - fmdry)\right)}{\pi}\right] - \left[0.5 + \frac{\arctan\left(epdry(S_{wr} - fmdry)\right)}{\pi}\right] \tag{A.7}$$

Table A.2
Relative permeability parameters used in the STARS simulation.

SWCON - Endpoint Saturation: Connate Water	0.204
SWCRIT - Endpoint Saturation: Critical Water	0.204
SOIRW - Endpoint Saturation: Irreducible Oil for Water-Oil Table	0.25
SORW - Endpoint Saturation: Residual Oil for Water-Oil Table	0.25
SOIRG - Endpoint Saturation: Irreducible Oil for Gas-Liquid Table	0
SORG - Endpoint Saturation: Residual Oil for Gas-Liquid Table	0
SGCON - Endpoint Saturation: Connate Gas	0.25
SGCRIT - Endpoint Saturation: Critical Gas	0.25
KROCW - *Kro* at Connate Water	0.5
KRWIRO - *Krw* at Irreducible Oil	0.14
KRGCL - *Krg* at Connate Liquid	0.47
KROGCG - *Krog* at Connate Gas	N/A
N_w - Exponent for calculating *Krw* from *KRWIRO*	5.25
N_{ow} - Exponent for calculating *Krow* from *KROCW*	5
N_{og} - Exponent for calculating *Krog* from *KROGCG*	5
N_g - Exponent for calculating *Krg* from *KRGCL*	1.22

APPENDIX B. Dimensionless time-distance (x_D vs t_D) diagrams of fractional-flow-theory calculations

In Table B.1 we present the saturations and mobilities of 20 characteristics out of the 500 we used in our fractional-flow theory calculations. The dimensionless time-distance (x_D-t_D) diagrams for gas injection are plotted in Fig. B.1 and for liquid injection are plotted in Fig. B.2. In all these diagrams we selected 7 of the 20 characteristics for illustration purposes. Fig. B.1 presents two plots: on the left the x_D-t_D diagram for gas injection excluding the *NZ* correction and, on the right, the x_D-t_D diagram for gas injection including the *NZ* correction. The mobilities of the characteristics next to the initial condition $S_{wI} = 1$ are of similar value in these two plots. However, the mobilities of the characteristics close to the injection condition ($S_{wr} = 0.204$) increase their mobility more rapidly when including the *NZ* correction (see also Table B.1).

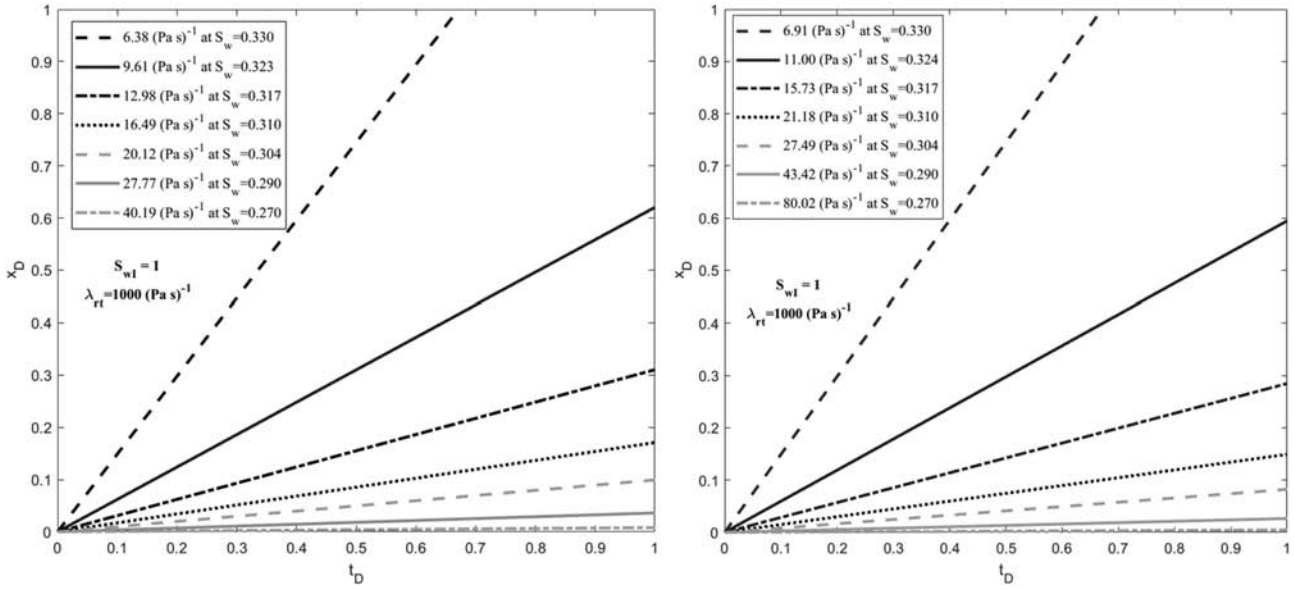


Fig. B.1. x_D vs t_D diagrams corresponding to gas injection excluding the *NZ* correction (on the left) and including the *NZ* correction (on the right). Values of total relative mobility in (Pa s) $^{-1}$ are given for the initial condition and selected characteristics.

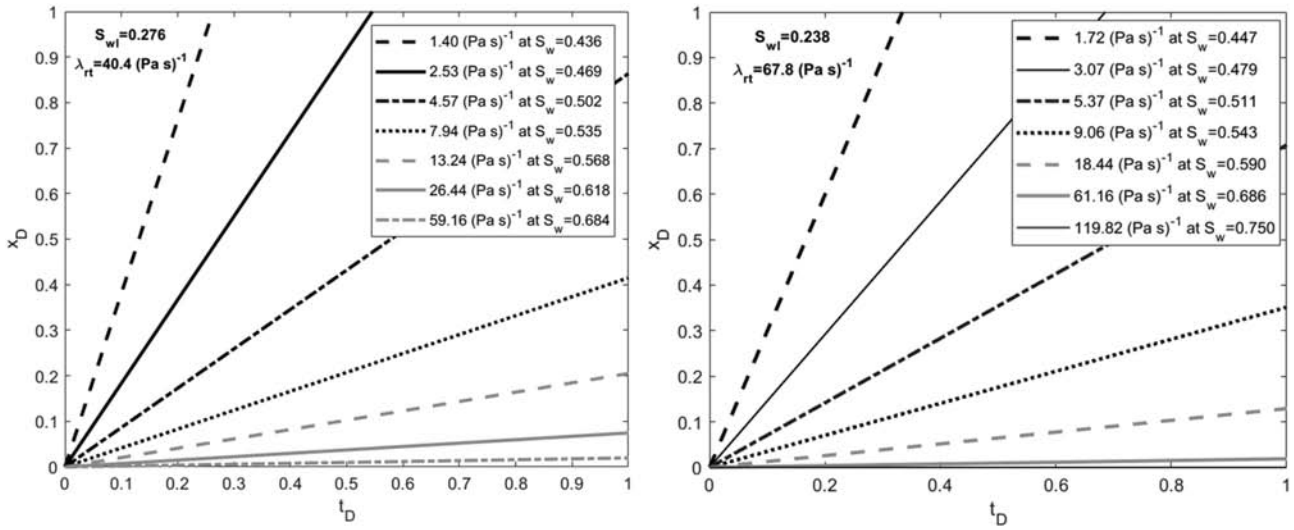


Fig. B.2. x_D vs t_D diagrams for liquid injection assuming an initial uniform water saturation on the left $S_{wI} = 0.276$ and on the right $S_{wI} = 0.238$. Values of total relative mobility in (Pa s) $^{-1}$ are given for the initial condition and selected characteristics.

Fig. B.2 presents the x_D-t_D diagram that corresponds to liquid injection assuming an initial water saturation S_{wi} of 0.34. This value was chosen because its mobility 4.68 $(Pa.s)^{-1}$ corresponds to an injectivity of approximately 213 units of dimensionless pressure, which is the average state at which foam mobility attains at the end of gas injection. From Table B.1 we observe that the largest total relative mobilities during gas injection correspond to the lowest water saturations. In contrast, during liquid injection the largest total relative mobilities correspond to the largest water saturations.

APPENDIX C. Summary of average dimensionless pressure from simulations and fractional-flow theory calculations.

The average dimensionless pressure is defined in Eq. (3) in the text. In Fig. C.1 we illustrate the physical meaning of *PD avg*. In this figure, the area of the rectangle with $P_{D\ avg} = 15.99$ is equal to area below the curve of the simulated P_D, in this example during gas injection when excluding the Peaceman equation and without grid refinement. In Table C.1 we summarize the average dimensionless pressure of each of the *FFT* calculations and of each of the *CMG's* simulations performed in this study. We observe that variations of up to 5 in the average dimensionless pressure can be attributed to the inherent numerical variations caused by slightly different initial conditions.

Table B.1
Total relative mobility (λ_{rt}) of the characteristics of the gas- and liquid-injection processes depicted in Fig. B.1 and in Fig. B.2.

Gas Injection			Liquid Injection			
STARS		NZ	STARS $S_{wI} = 0.276$		NZ $S_{wI} = 0.238$	
S_w	λ_{rt}	λ_{rt}	S_w	λ_{rt}	S_w	λ_{rt}
	$(Pa\ s)^{-1}$	$(Pa\ s)^{-1}$		$(Pa\ s)^{-1}$		$(Pa\ s)^{-1}$
0.211	89.92	1868.66	0.404	0.83	0.447	1.72
0.217	84.37	903.15	0.422	1.08	0.463	2.30
0.224	78.94	569.04	0.440	1.47	0.479	3.07
0.231	73.65	400.11	0.458	2.04	0.495	4.08
0.237	68.48	298.49	0.477	2.83	0.511	5.37
0.244	63.45	230.87	0.495	3.92	0.527	7.01
0.250	58.54	182.80	0.513	5.38	0.543	9.06
0.257	53.76	147.01	0.531	7.29	0.559	11.59
0.264	49.11	119.44	0.550	9.74	0.575	14.69
0.270	44.59	97.63	0.568	12.86	0.590	18.44
0.277	40.19	80.02	0.586	16.76	0.606	22.95
0.284	35.92	65.56	0.604	21.60	0.622	28.33
0.290	31.78	53.53	0.622	27.53	0.638	34.70
0.297	27.77	43.42	0.641	34.73	0.654	42.20
0.304	23.88	34.83	0.659	43.40	0.670	50.97
0.310	20.12	27.49	0.677	53.75	0.686	61.16
0.317	16.49	21.18	0.695	66.03	0.702	72.95
0.323	12.98	15.73	0.714	80.49	0.718	86.52
0.330	9.61	11.00	0.732	97.43	0.734	102.07
0.337	6.38	6.91	0.750	117.15	0.750	119.82

Table C.1
Average dimensionless pressure $P_{D\ avg}$ of the simulations and *FFT* calculations performed in this study.

Method	Grid Refinement	$P_{D\ avg}$ for Gas Injection	$P_{D\ avg}$ for Liquid Injection
Fractional-flow theory		37	49
STARS			
Fractional-flow theory including the *NZ* correction		27	46
Simulations including the Peaceman model	Original	133	139
	3 × 3	68	70
	5 × 5	57	61
	7 × 7	51	57
Simulations including both the Peaceman model and the *NZ* correction	Original	104	144
	3 × 3	46	73
	5 × 5	36	63
	7 × 7	32	60
	17 × 17	26	56
Simulations excluding both the Peaceman model and the *NZ* correction	3 × 3	48	55
	5 × 5	45	54
	7 × 7	43	53
Simulations excluding foam in the well grid block	3 × 3	38	49
	5 × 5	37	49
	7 × 7	36	50

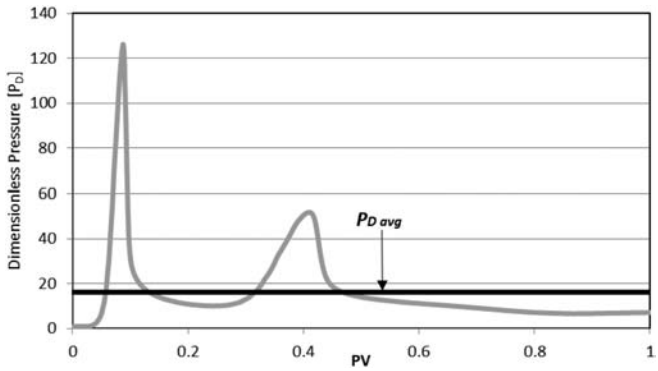


Fig. C.1. Illustration of the physical meaning of the average dimensionless pressure $P_{D\,avg}$ during gas injection in a simulation using the grid without refinement and excluding the Peaceman equation.

APPENDIX D. Radial inflow well model (Peaceman model) and numerical solver settings

In STARS (Computer modelling group, 2016) the well model gives the increase in well pressure over the average pressure of the grid block where the well is placed. To this end, the Peaceman model (Peaceman, 1978) incorporates an effective outer radius, and in this manner the radial-flow equation is solved between the effective outer radius (r_o) and the wellbore radius (r_w). In our simulations the outflow (q) in the grid block is related to the pressure drop according to the following equation

$$q = I\,\lambda_{rt}(P_{well} - P_{or}) \tag{D.1}$$

where I, λ_{rt}, P_{well}, and P_{or} denote the well index, the total relative mobility, the pressure rise at the well and the pressure rise in the grid block, respectively.

The well index I corrects for the appropriate pressure drop depending on the boundary conditions and the location of the well within the grid block using the following expression:

$$I = \frac{2\,\pi\,h\,k\,f_h\,f}{\ln(r_o/r_w) + S} \tag{D.2}$$

where h, k, f_h, f, r_o, r_w, and S denote the layer thickness, the permeability, layer thickness factor, well fraction factor, the outer radius, the wellbore radius and the skin factor, respectively. In our simulations, $h = 10$ m, $k = 150$ mD, $f_h = 1$, $r_w = 0.1$ m, and $S = 0$.

In our simulations the outer radius is calculated as follows:

$$r_o = CC\sqrt{\frac{\Delta x^2 + \Delta y^2}{f\,\pi}} \tag{D.3}$$

where $CC, f, \Delta x^2$ and Δy^2 are the geometric factor depending on well location, the well fraction factor, the grid block sizes in the plane perpendicular to the well. In our simulations, the location of the well in the reservoir and within the grid block in our simulations require CC and f to be equal to 0.249 and 1, respectively.

In the simulations that do not include the Peaceman Model, we calculate the pressure drop by taking the grid block pressure instead of the well pressure. Most of the numerical settings in the simulations used the default value to keep our simulation as general as possible. However, we modified some of the numerical settings of the solver to warrant the convergence of all our simulations. We modified the following setting for the timestep control (DTMAX) of 0.25 days, a minimum step size (DTMIN) of 1×10^{-5} days and the same value for the first time step size after well change (DTWELL). The maximum pressure limit (MAXPRES) was also changed to 1×10^{9} kPa. For the solution method we used UPSTREAM = NLEVEL. And the linear solver precision (PRECC) was set to 1×10^{-3}.

References

Agada, S., Soni, K., Geiger, S., 2015. Numerical simulation of foam EOR processes in heterogeneous fractured carbonate reservoirs. In: IOR 2015-18th European Symposium on Improved Oil Recovery. European Association of Geoscientists & Engineers. https://doi.org/10.3997/2214-4609.201412138.

Al Ayesh, A.H., Salazar, R., Farajzadeh, R., Vincent-Bonnieu, S., Rossen, W.R., 2017. Foam diversion in heterogeneous reservoirs: effect of permeability and injection method. SPE J. 22, 1402–1415. https://doi.org/10.2118/179650-PA.

AlMaqbali, A., Agada, S., Geiger, S., Haugen, Å., Fernø, M.A., 2015. Modelling foam displacement in fractured carbonate reservoirs. In: Abu Dhabi International Petroleum Exhibition and Conference, Abu Dhabi, UAE. https://doi.org/10.2118/177600-MS.

Ashoori, E., Van Der Heijden, T.L.M., Rossen, W.R., 2010. Fractional-flow theory of foam displacements with oil. SPE J. 15 (2), 260–273. https://doi.org/10.2118/121579-PA.

Aziz, K., Settari, T., 1979. Petroleum Reservoir Simulation. Applied Science Publishers, London.

Blaker, T., Marten, G.A., Skauge, A., Rasmuussen, L., Celius, H.K., Martinsen, H.A., Vassenden, F., 2002. Foam for gas mobility control in the snorre field: the FAWAG project. SPE Reservoir Eval. Eng. 5 (4), 317–323. https://doi.org/10.2118/78824-PA.

Boeije, C.S., Rossen, W.R., 2015a. Fitting foam-simulation-model parameters to data: I. Coinjection of gas and liquid. SPE Reservoir Eval. Eng. 18, 264–272. https://doi.org/10.2118/174544-PA.

Boeije, C.S., Rossen, W.R., 2015b. Gas-injection rate needed for SAG foam processes to overcome gravity override. SPE J. 20, 49–59. https://doi.org/10.2118/166244-PA.

Buckley, S.E., Leverett, M.C., 1942. Mechanism of fluid displacement in sands. Trans. Soc. Petrol. Eng. 146 (Part 1), 107–116. https://doi.org/10.2118/942107-G.

Cheng, L., Reme, A.B., Shan, D., Coombe, D.A., Rossen, W.R., 2000. Simulating foam processes at high and low foam qualities. In: SPE/DOE Improved Oil Recovery Symposium. Society of Petroleum Engineers. https://doi.org/10.2118/59287-MS.

Chengjun, W., Jun, N., Shaojing, J., et al., 2022. Rapid evaluation model for EOR techniques applicability of gas flooding, foam flooding and surfactant flooding based on modified fractional flow theory. J. Pet. Explor. Prod. Technol. 1–13. https://doi.org/10.1007/s13202-022-01591-1.

Computer Modelling Group Ltd, 2016. CMG-STARS User's Guide. CMG.

Dholkawala, Z.F., Sarma, H.K., Kam, S.I., 2007. Application of fractional flow theory to foams in porous media. J. Petrol. Sci. Eng. 57 (1–2), 152–165. https://doi.org/10.1016/j.petrol.2005.10.012.

Eftekhari, A.A., Farajzadeh, R., 2017. Effect of foam on liquid phase mobility in porous media. Sci. Rep. 7, 43870. https://doi.org/10.1038/srep43870.

Gong, J., Vincent-Bonnieu, S., Kamarul Bahrim, R.Z., Che Mamat, C.A., Tewari, R.D., Groenenboom, J., Farajzadeh, R., Rossen, W.R., 2019. Modeling of liquid injectivity in surfactant-alternating-gas foam enhanced oil recovery. SPE J. 24 (3), 1123–1138. https://doi.org/10.2118/190435-PA.

Gong, J., Vincent-Bonnieu, S., Kamarul Bahrim, R.Z., Che Mamat, C.A.N.B., Groenenboom, J., Farajzadeh, R., Rossen, W.R., 2020a. Laboratory investigation of liquid injectivity in surfactant-alternating-gas foam enhanced oil recovery. Transport Porous Media 131 (1), 85–99. https://doi.org/10.1007/s11242-018-01231-5.

Gong, J., Martinez, W.F., Vincent-Bonnieu, S., Bahrim, R.Z.K., Mamat, C.A.N.B.C., Tewari, R.D., Amir, M.I.M., Farajzadeh, R., Rossen, W., 2020b. Effect of superficial velocity on liquid injectivity in SAG foam EOR. Part 1: experimental study. Fuel 278, 118299. https://doi.org/10.1016/j.fuel.2020.118299.

Gong, J., Wang, Y., Bahrim, R.Z.B., Tewari, R.D., Amir, M.I.M., Farajzadeh, R., Rossen, W., 2024. Liquid injectivity in a SAG foam process: effect of permeability. Pet. Sci. 21 (1), 302–314. https://doi.org/10.1016/j.petsci.2023.10.010.

Heller, J.P., 1994. CO_2 foams in enhanced oil recovery. In: Schramm, L.L. (Ed.), Foams: Fundamentals and Applications in the Petroleum Industry. American Chemical Society, Washington, DC, USA. https://doi.org/10.1021/ba-1994-0242.ch005.

Jamshidnezhad, M., Shen, C., Kool, P., Mojaddam Zadeh, A., Rossen, W.R., 2010. Improving injectivity to fight gravity segregation in gas enhanced oil recovery. SPE J. 15, 91–104. https://doi.org/10.2118/112375-PA.

Kazemi Nia Korrani, A., Jerauld, G.R., 2022. Upscaling low-salinity benefit from laboratory scale to field scale: an ensemble of models with a relative permeability uncertainty range. SPE J. 27 (6), 3674–3687. https://doi-org.tudelft.idm.oclc.org/10.2118/209412-PA.

Khatib, Z.I., Hirasaki, G.J., Falls, A.H., 1988. Effects of Capillary Pressure on Coalescence and Phase Mobilities in Foams Flowing Through Porous Media. Society of Petroleum Engineers. https://doi.org/10.2118/15442-PA. SPE-15442-PA 3(03).

Kovscek, A.R., Patzek, T.W., Radke, C.J., 1995. A mechanistic population balance model for transient and steady-state foam flow in Boise sandstone. Chem. Eng. Sci. 50 (23), 3798–3799. https://doi.org/10.1016/0009-2509(95)00199-F.

Kuehne, D.L., Ehman, D.I., Emanuel, A.S., Magnani, C.F., 1990. Design and evaluation of a nitrogen-foam field trial. J. Petrol. Technol. 42 (2), 504–512. https://doi.org/10.2118/17381-PA.

Lake, L., Johns, R.T., Rossen, W.R., Pope, G.A., 2014. Fundamentals of Enhanced Oil Recovery. Society of Petroleum Engineers, Richardson, Texas.

Leeftink, T.N., Latooij, C.A., Rossen, W.R., 2015. Injectivity errors in simulation of foam EOR. J. Petrol. Sci. Eng. 126, 26–34. https://doi.org/10.1016/j.petrol.2014.11.026.

Luo, H., Delshad, M., Zhao, B., Kishore, K.M., 2017. A fractional flow theory for unstable immiscible floods. In: SPE Canada Heavy Oil Technical Conference. https://doi.org/10.2118/184996-MS. Calgary, Alberta, Canada.

Martinsen, H.A., Vassenden, F., 1999. Foam-assisted water alternating gas (FAWAG) process on snorre. In: European IOR Symposium. https://doi.org/10.3997/2214-4609.201406335. Brighton, UK.

Masoudi, R., Ann Giddins, M., Karkooti, H., Jalan, S., Valero Gil, A. A., 2015. Foam simulation from coreflood to field scale. In: SPE Asia Pacific Enhanced Oil Recovery Conference.

Mayberry, D.J., Afsharpoor, A., Kam, S.I., 2008. The use of fractional-flow theory for foam displacement in presence of oil. SPE Reservoir Eval. Eng. 11 (4), 707–718. https://doi.org/10.2118/100964-PA.

Mukherjee, J., Norris, S.O., Nguyen, Q.P., Scherlin, J.M., Vanderwal, P.G., Abbas, S., 2015. CO_2 foam pilot in salt creek field, Natrona County, WY-Phase I-Laboratory work, reservoir simulation, and initial design. In: IOR 2015-18th European Symposium on Improved Oil Recovery. European Association of Geoscientists & Engineers. https://doi.org/10.2118/169166-MS.

Namdar Zanganeh, M., Kraaijevanger, J.F.B.M., Buurman, H.W., Jansen, J.D., Rossen, W.R., 2014. Challenges to adjoint-based optimization of a foam EOR process. Comput. Geosci. 18 (3–4), 563–577. https://doi.org/10.1007/s10596-014-9412-4.

Noh, M., Lake, L.W., Bryant, S.L., Araque-Martinez, A., 2007. Implications of coupling fractional flow and geochemistry for CO2 injection in aquifers. SPE Reservoir Eval. Eng. 10 (4), 406–414. https://doi-org.tudelft.idm.oclc.org/10.2118/89341-PA.

Orujov, A., Coddington, K., Aryana, S.A., 2023. A review of CCUS in the context of foams, regulatory frameworks and monitoring. Energies 16, 3284. https://doi.org/10.3390/en16073284.

Peaceman, D.W., 1978. Interpretation of well-block pressures in numerical reservoir simulation (includes associated paper 6988). SPE J. 18 (3), 183–194. https://doi.org/10.2118/6893-PA.

Pope, G.A., 1980. The application of fractional flow theory to enhanced oil recovery. SPE J. 20 (3), 191–205. https://doi.org/10.2118/7660-PA.

Quinelato, T.O., de Paula, F.F., Igreja, I., Lozano, L.F., Chapiro, G., 2022. On the injectivity estimation in foam EOR. J. Pet. Explor. Prod. Technol. 12, 2723–2734. https://doi.org/10.1007/s13202-022-01474-5.

Redlich, O., Kwong, J.N., 1949. On the thermodynamics of solutions. V. An equation of state. Fugacities of gaseous solutions. Chem. Rev. 44 (1), 233–244.

Rossen, W.R., 1996. Foams in enhanced oil recovery. In: Prud'homme, R.K., Khan, S. (Eds.), Foams: Theory, Measurements and Applications. Marcell Dekker.

Rossen, W.R., Farajzadeh, R., Hirasaki, G.J., Amirmoshiri, M., 2022. Potential and challenges of foam-assisted CO_2 sequestration. In: SPE Improved Oil Recovery Conference. https://doi.org/10.2118/209371-MS. Tulsa, OK.

Salazar Castillo, R.O., Rossen, W.R., 2020. Scaleup of laboratory data for surfactant-alternating-gas foam enhanced oil recovery. SPE J. 25, 1857–1870. https://doi.org/10.2118/201204-PA.

Salazar Castillo, R.O., Ter Haar, S.F., Ponners, C.G., Bos, M., Rossen, W.R., 2019. Fractional-flow theory for non-newtonian surfactant-alternating-gas foam processes. Transport Porous Media 131, 399–426. https://doi.org/10.1007/s11242-019-01351-6.

Schmid, K.S., Alyafei, N., Geiger, S., Blunt, M.J., 2016. Analytical solutions for spontaneous imbibition: fractional-flow theory and experimental analysis. SPE J. 21, 2308–2316. https://doi.org/10.2118/184393-PA.

Shan, D., Rossen, W.R., 2004. Optimal injection strategies for foam IOR. SPE J. 9 (2), 132–150. https://doi.org/10.2118/88811-PA. SPE-88811-PA.

Sharma, M., 2019. CO_2 Mobility Control with Foam for Enhanced Oil Recovery and Associated Storage multi-scale Approach for Field Application (Ph.D. Dissertation). University of Stavanger, Norway.

Sharma, M., Alcorn, Z.P., Fredriksen, S., Fernø, M., Graue, A., 2017. Numerical modelling study for designing CO2-foam field pilot. In: IOR 2017-19th European Symposium on Improved Oil Recover. European Association of Geoscientists & Engineers. https://doi.org/10.3997/2214-4609.201700339.

Tang, J., Castañeda, P., Marchesin, D., Rossen, W.R., 2019. Three-phase fractional-flow theory of foam-oil displacement in porous media with multiple steady states. Water Resour. Res. 55 (12), 10319–10339. https://doi.org/10.1029/2019WR025264.

Walsh, M.P., Lake, L.W., 1989. Applying fractional flow theory to solvent flooding and chase fluids. J. Petrol. Sci. Eng. 2 (4), 281–303. https://doi.org/10.1016/0920-4105(89)90005-3.

Wu, Q., Ding, L., Zhang, L., Ge, J., Rahman, M.A., Economou, I.G., Guérillot, D., 2023. Polymer enhanced foam for improving oil recovery in oil-wet carbonate reservoirs: a proof of concept and insights into the polymer-surfactant interactions. Energy 264, 126256. https://doi.org/10.1016/j.energy.2022.126256.

Zeilinger, S.C., Shi, J.X., Lim, M.T., Rossen, W.R., 1995. Simplified mechanistic modelling of foam processes for improved oil recovery. In: IOR 1995-8th European Symposium on Improved Oil Recovery. European Association of Geoscientists & Engineers. https://doi.org/10.3997/2214-4609.201406961.

Zhou, Z.H., Rossen, W.R., 1995. Applying fractional-flow theory to foam processes at the limiting capillary pressure. SPE Adv. Technol. 3 (1), 154–162. https://doi.org/10.2118/24180-PA.